

A High-Performance Nanoreactor for Carbon-Oxygen Bonds Hydrogenation Reactions Achieved by the Morphology of Nanotube-Assembled Hollow Sphere

Dawei Yao, Yue Wang, Ying Li, Yujun Zhao, Jing Lv, and Xinbin Ma

ACS Catal., Just Accepted Manuscript • DOI: 10.1021/acscatal.7b03026 • Publication Date (Web): 27 Dec 2017

Downloaded from <http://pubs.acs.org> on December 27, 2017

Just Accepted

“Just Accepted” manuscripts have been peer-reviewed and accepted for publication. They are posted online prior to technical editing, formatting for publication and author proofing. The American Chemical Society provides “Just Accepted” as a free service to the research community to expedite the dissemination of scientific material as soon as possible after acceptance. “Just Accepted” manuscripts appear in full in PDF format accompanied by an HTML abstract. “Just Accepted” manuscripts have been fully peer reviewed, but should not be considered the official version of record. They are accessible to all readers and citable by the Digital Object Identifier (DOI®). “Just Accepted” is an optional service offered to authors. Therefore, the “Just Accepted” Web site may not include all articles that will be published in the journal. After a manuscript is technically edited and formatted, it will be removed from the “Just Accepted” Web site and published as an ASAP article. Note that technical editing may introduce minor changes to the manuscript text and/or graphics which could affect content, and all legal disclaimers and ethical guidelines that apply to the journal pertain. ACS cannot be held responsible for errors or consequences arising from the use of information contained in these “Just Accepted” manuscripts.



1
2
3
4
5
6
7 A High-Performance Nanoreactor for Carbon-Oxygen Bonds
8 Hydrogenation Reactions Achieved by the Morphology of
9 Nanotube-Assembled Hollow Sphere
10
11
12
13
14
15

16 *Dawei Yao[‡], Yue Wang[‡], Ying Li, Yujun Zhao, Jing Lv and Xinbin Ma**
17
18
19

20 Key Laboratory for Green Chemical Technology of Ministry of Education, Collaborative
21
22

23 Innovation Center of Chemical Science and Engineering
24
25

26 School of Chemical Engineering and Technology, Tianjin University
27
28

29 Tianjin 300072 (P. R. China)
30
31

32 ABSTRACT: Hydrogenation of carbon-oxygen bonds are extensively used in organic synthesis.
33
34 However, a high partial pressure of hydrogen or the presence of excess hydrogen is usually
35
36 essential to achieve favorable conversions. In addition, because most hydrogenations are
37
38 consecutive reactions, the selectivity is difficult to manipulate, leading to an unsatisfactory
39
40 distribution of product. Herein, a copper silicate nanoreactor with a nanotube-assembled hollow
41
42 sphere (NAHS) hierarchical structure is proposed as a solution to these problems. In the case of
43
44 dimethyl oxalate (DMO) hydrogenation, the NAHS nanoreactor achieves remarkable catalytic
45
46 activity (the yield of ethylene glycol is 95%) and stability (> 300 h) when the H₂/DMO molar
47
48 ratio is as low as 20 (compared to typical values of 80 to 200). For further investigation,
49
50
51
52
53
54
55
56
57
58
59
60

1
2
3
4 nanotubes and lamellar-shaped Cu/SiO₂ catalysts with similar surface areas of active sites of
5
6 NAHS were investigated as contrasts. Combining the high-pressure hydrogen adsorption and
7
8 Monte Carlo simulation, it is demonstrated that hydrogen can enrich on the concave surface of
9
10 nanotube and hollow sphere, leading to a favorable activity in such a low H₂ proportion.
11
12 Furthermore, because of the spatial restriction effect of reactants, adjusting the diffusion path is
13
14 an effective route for manipulating the selectivity and product distribution of the hydrogenation
15
16 reactions. By varying the length of nanotubes on NAHS, the yields of methyl glycolate and
17
18 ethylene glycol are easily to control. The NAHS nanoreactor, with insights into the effect of
19
20 morphology on hydrogen enrichment and spatial restriction of reactants diffusion, offers
21
22 inspiring possibilities in the rational design of catalysts for the hydrogenation reactions.
23
24
25
26
27
28
29
30

31
32
33 Keywords: enrichment • heterogeneous catalysis • hydrogenation • copper-based catalyst •
34
35 spatial restriction
36
37

38 39 INTRODUCTION

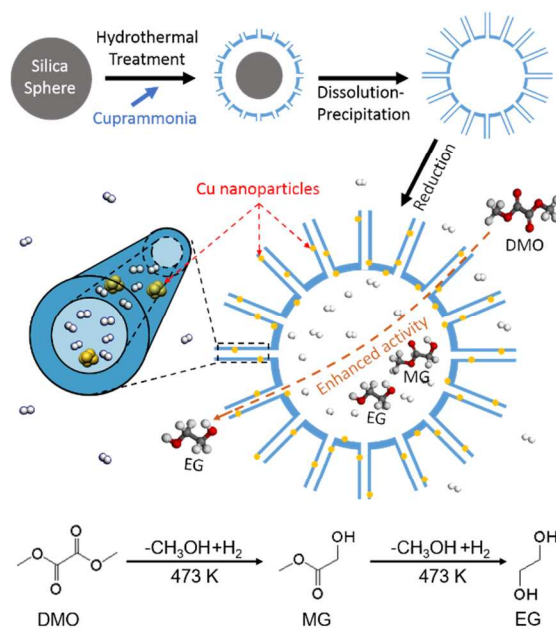
40
41 Hydrogenation of carbon-oxygen (C=O/C-O) bonds (for example, esters, ethers, furfural and
42
43 CO₂), as a versatile fundamental reaction, has been extensively used in chemical synthesis.
44
45 Numerous attractive chemical products, fuels and polymers can be obtained by the
46
47 hydrogenation of C=O/C-O from coal-derived resources or biomass.¹⁻³ However, two common
48
49 issues are desiderating to be overcome in these hydrogenation reactions, especially for industrial
50
51 applications. First, a high partial pressure of H₂ or the presence of excess H₂ (much higher than
52
53
54
55
56
57
58
59
60

1
2
3
4 the stoichiometric ratio) is an essential requirement for obtaining favorable conversion and/or
5
6 selectivity in the reaction. For example, the H₂ pressures required in most biomass
7
8 hydrogenations are as high as 4-10 MPa, some even reaching 100 MPa.² In the synthesis of
9
10 ethylene glycol (EG) from syngas via the hydrogenation of dimethyl oxalate (DMO), the
11
12 H₂/DMO ratio is typically higher than 80 to generate favorable space time yield of EG.⁴⁻⁵
13
14
15 Although a few cases were conducted at the H₂/DMO ratio of 50, the space velocities of DMO
16
17 were all very low.⁶⁻⁷ Consequently, recycling large amounts of high-pressure H₂ is necessary in
18
19 these processes, which leads to massive energy consumption and requires high-cost industrial
20
21 devices. Second, because most hydrogenations are consecutive reactions, such as hydrogenation
22
23 of furfural, DMO or biomass-derived glyceride compounds, the selectivity of product is difficult
24
25 to manipulate. As a result, the cost of separation is increased and the yields of products are
26
27 reduced, which greatly hinders the application of these hydrogenations in industry.^{2, 8-9}
28
29
30 Therefore, developing innovative and practical methods to overcome these two problems is
31
32 imperative.
33
34
35
36
37
38
39
40
41

42 One direction toward finding a solution to these challenges is the rational design of catalysts. A
43
44 unique morphology that enables the enrichment of H₂ may provide a way to maintain the
45
46 catalytic performance with reduced H₂ concentrations in feed. Small molecules such as H₂, CO
47
48 or CO₂ can be effectively adsorbed by materials with a nanotube or hollow structure.¹⁰⁻¹¹
49
50
51 Additionally, specific morphologies, such as the core-shell structure, have been used to isolate
52
53 active sites and for sequential channeling of reactants and intermediates, resulting in direct
54
55
56
57
58
59
60

1
2
3
4 synthesis of products in a consecutive reaction. Such results demonstrate the importance of
5
6 spatial restriction for product control.¹²⁻¹⁴ Thus, designing and fabricating catalysts with a
7
8 particular morphology with the aforementioned characteristics may be a promising strategy to
9
10 simultaneously address both of the problems associated with hydrogenation.
11
12

13
14
15 Herein, we report a facile and efficient approach for the fabrication of a nanoreactor with
16
17 unique morphology of nanotube-assembled hollow sphere (NAHS), attempting to solve both of
18
19 the aforementioned issues. DMO as the simplest di-ester containing C=O, C-O and C-C bonds,
20
21 becomes a typical case to understand the hydrogenation of these bonds. Moreover, this reaction
22
23 not only comprises two continuous hydrogenations (Scheme 1), including the hydrogenation of
24
25 DMO to methyl glycolate (MG) followed by a further hydrogenation to EG, but also typically
26
27 needs a high H₂/DMO ratio of 80-200 to reach satisfied activity and selectivity.^{3, 15} Thus, DMO
28
29 hydrogenation became a showcase to allow us to investigate the effect of morphology on activity
30
31 and selectivity. We here demonstrate the product distribution can be simply controlled by
32
33 adjusting the length of nanotubes on NAHS, as well as remarkable efficiency and stability at
34
35 H₂/DMO ratio of 20 is achieved by this NAHS nanoreactor. The superior activity and adjustable
36
37 selectivity is attributed to the effect of unique morphology on enrichment of hydrogen within the
38
39 nanoreactor and spatial restriction of reactants, respectively.
40
41
42
43
44
45
46
47
48
49
50
51
52
53
54
55
56
57
58
59
60



Scheme 1. Scheme of nanotube-assembled hollow sphere nanoreactor for DMO hydrogenation.

EXPERIMENTAL SECTION

Materials

All the chemicals and reagents were analytical grade and used without any purification. $\text{Cu}(\text{NO}_3)_2 \cdot 3\text{H}_2\text{O}$ (99 %) was purchased from Sinopharm Chemical Reagent Co. Tetraethyl orthosilicate (98 %), ammonia (25 wt. % in water), HNO_3 (68 wt. %), NH_4NO_3 (99.8 %), dehydrated methanol (99.8 %) and dehydrated ethanol (99.8 %) were all purchased from Tianjin Kemiou Chemical Reagent Co.

Catalyst preparation

Given mesoporous copper silicate has been reported as an excellent catalyst precursor for DMO hydrogenation³, the copper silicate NAHS materials was fabricated here by using the modified hydrothermal method¹⁶⁻¹⁷ (Scheme 2).

1
2
3
4 Synthesis of the silica spheres: Monodispersed silica spheres were fabricated according to the
5
6 Stöber method. Briefly, 9 mL ammonia was added into 25 mL deionized water, followed by the
7
8 addition of a mixture of 8 mL tetraethyl orthosilicate (TEOS) and dehydrated ethanol. The
9
10 mixture was then stirred at 313 K for 2 h to obtain the silica sphere solution. The silica spheres
11
12 were separated by centrifugation and washed with ethanol and deionized water. Finally, the silica
13
14 spheres were dispersed into 60 mL deionized water again for the copper silicate materials
15
16 preparation process.
17
18
19
20
21
22

23 Fabrication of the copper silicate NAHS: Typically, 2.42 g copper nitrate and 13 mL ammonia
24
25 were added into 200 mL deionized water, followed by drop-wise addition of 60 mL silica
26
27 spheres solution with stirring and then aged at 313 K for 3 h. The mixture was transferred into an
28
29 autoclave, heated at 413 K for 5 h to prepare the NAHS materials with approximately 63
30
31 nm-length nanotubes (denoted as NAHS-63nm). The NAHS-70nm, NAHS-92nm, NAHS-119nm
32
33 materials were fabricated by increasing the hydrothermal treatment time to 10 h, 15 h and 20 h,
34
35 respectively. Likewise, the NAHS-120nm and NAHS-232nm were similarly fabricated with an
36
37 increased mass of copper nitrate addition to 7.11 g, and by modifying the hydrothermal treatment
38
39 time to 5 h and 20 h, respectively. The obtained materials were separated by centrifugation,
40
41 washed with deionized water until the pH value reached 7.0, and dried under vacuum at 355 K
42
43 for 6 h. These as-synthesized samples were calcined in static air at 723 K for 4 h, tableted,
44
45 crushed, and sieved to 40–60 meshes.
46
47
48
49
50
51
52
53
54
55
56
57
58
59
60

1
2
3
4 Preparation of the copper silicate nanotubes (NTs): Typically, 7.11 g copper nitrate and 13 mL
5
6 ammonia with calculated proportion were mixed into deionized water, followed by drop-wise
7
8 addition of 60 mL silica spheres solution with stirring. After aging at 313 K for 3 h, the 5 g
9
10 NH_4NO_3 was added. Then, the mixture was transferred into an autoclave and heated at 413 K for
11
12 several hours. The product was separated by centrifugation, washed until the pH value reached
13
14 7.0 and dried under vacuum at 355 K for 6 h. This as-synthesized sample was calcined in static
15
16 air at 723 K for 4 h, tableted, crushed, and sieved to 40–60 meshes.
17
18
19
20
21
22

23 Preparation of the lamellar-structured Cu/SiO₂: The lamellar-structured Cu/SiO₂ was prepared
24
25 by using the ammonia evaporation (AE) method. Typically, copper nitrate and ammonia with
26
27 calculated proportion were mixed into deionized water and stirred for 10 min, followed by a
28
29 drop-wise addition of silica sol while stirring. Then, the suspension was stirred at room
30
31 temperature for 6 h. The initial pH value of the suspension was 11-12. The suspension was
32
33 subsequently heated in a 353 K water bath to allow the evaporation of ammonia, the decrease of
34
35 pH, and the consequent deposition of copper species on silica. When the pH value decreased to
36
37 7, the evaporation process was terminated. The product was washed, filtrated and dried under
38
39 vacuum at 355 K for 6 h. This as-synthesized sample was calcined in static air at 723 K for 4 h,
40
41 tableted, crushed, and sieved to 40–60 meshes.
42
43
44
45
46
47
48
49

50 **Catalytic activity test**

51
52 The catalytic evaluation was carried out in a fixed-bed reaction system. A sample of 0.4 g of
53
54 catalyst (40-60 meshes) was placed in the certain zone of the reaction tube where the temperature
55
56
57
58
59
60

1
2
3
4 could maintain constant. Before the reaction, the catalyst was first reduced by hydrogen at 573 K
5
6
7 for 4 h. Then, the feed (20 wt. % DMO, dissolved in methanol) was injected into the fixed-bed
8
9
10 reaction system contiguously with a certain weight liquid hourly space velocity (WLHSV). The
11
12 catalytic performance was tested at 473 K under 2.5 MPa. The reaction products were
13
14 condensed, then analyzed on the Agilent Micro GC 6820, which is equipped with a
15
16 HP-INNOWAX capillary column (Hewlett-Packard Company, 30 m×0.32 mm×0.50 μm), as
17
18 well as a flame ionization detector (FID).
19
20
21
22

23 **Characterization**

24
25 Pore structure of the catalysts was determined at 77 K by a N₂ adsorption-desorption method
26
27 using a Micromeritics Tristar II 3000 Analyzer. Pore-size distribution was estimated by the
28
29 Barrett-Joyner-Halenda (BJH) method from adsorption isotherm branch of the isotherms, and the
30
31 specific surface area was calculated from the isotherms using Brunauer–Emmett–Teller (BET)
32
33 method.
34
35
36
37
38

39 The copper content of catalyst was analyzed by using an Inductively Coupled Plasma Optical
40
41 Emission Spectrometer (ICP-OES, Varian Vista-MPX), and was determined by the Cu
42
43 characteristic peak at 324.754 nm.
44
45
46

47 Transmission electron microscopy (TEM) image was analyzed by using a Philips TECNAI G2
48
49 F20 system electron microscope. The 40-60 meshes sample was crushed and dispersed in
50
51 ethanol, dropped onto a copper grid-supported carbon membrane and dried. For each NAHS
52
53 material and NTs material, 100-200 nanotubes were measured to obtain the length distribution of
54
55
56
57
58
59
60

1
2
3
4 nanotubes. Likewise, for each catalyst, 200-300 copper nanoparticles were processed to calculate
5
6
7 the average particle size.

8
9 Scanning electron microscopy (SEM) image was analyzed by using a Hitachi S-4800 system
10
11
12 electron microscope. The calcined sample was severely crushed and dispersed in ethanol,
13
14
15 dropped onto small pieces of quartz glass.

16
17 The copper dispersion and metallic copper surface area were measured by N₂O titration using a
18
19
20 Micromeritics Autochem II 2920 apparatus. Briefly, 50 mg sample was pretreated in Ar for 1 h
21
22
23 at 473 K, followed by its reduction in 10% H₂/Ar flow for 2 h at 573 K. Subsequently, the
24
25
26 sample was exposed to N₂O for 1 h at 363 K, which could ensure that the surface metallic copper
27
28
29 was completely oxidized to Cu₂O. After purging the remaining N₂O with a flow of Ar for 30
30
31
32 min, the sample was reduced again at 573 K by pulse titration using 10% H₂/Ar.

33
34 X-ray diffraction (XRD) was conducted with a Rigaku C/max-2500 diffractometer, employing
35
36
37 the graphite-filtered Cu K α radiation ($\lambda=1.5406 \text{ \AA}$) at room temperature. The particle size of
38
39
40 copper was calculated according to the Scherrer equation. The reduced catalyst powder was
41
42
43 scanned with a rate of 8°/min from 2 θ ranging from 10° to 90°.

44
45 Fourier-transform Infrared (FTIR) spectra was recorded by a Nicolet 6700 spectrometer
46
47
48 equipped with a DTGS detector in the range of 400-4000 cm⁻¹. The sample was ground,
49
50
51 dispersed in KBr, and pelletized. The spectral resolution was 4 cm⁻¹, and 32 scans were recorded
52
53
54 for each spectrum.

1
2
3
4 The in situ FTIR of CO adsorption was performed to determine the surface area of Cu^+ species
5
6 using the Nicolet 6700 spectrometer equipped with a MCT/A detector and a vacuum system.
7
8 Briefly, the sample (16-17 mg) was tableted and placed into the in situ cell. Subsequently, the
9
10 sample disk was reduced under a 10% H_2/Ar flow at 573 K for 1 h, then exposed to the flow of
11
12 CO at 303 K for 30 min. In order to remove CO molecules in the gas phase and the ones that
13
14 were weakly adsorbed on the sample, an evacuation was performed until the scanned spectra no
15
16 longer changed.
17
18
19
20
21
22

23 X-ray photoelectron spectra (XPS) and Auger electron spectroscopy (AES) were detected on a
24
25 Kratos XSAM 800 spectrometer with Al $\text{K}\alpha$ X-ray radiation source ($h\nu = 1486.6$ eV). The
26
27 sample was tableted to a small disk, reduced in H_2 at 573 K for 4 h, immediately transferred into
28
29 the chamber, and vacuumed under 10^{-8} Torr. The obtained binding energy was calibrated using
30
31 the Si 2p peak at 103.2 eV as the reference. The experimental error was within ± 0.2 eV.
32
33
34
35

36 The high-pressure hydrogen adsorption was carried out on a pressure composition isothermal
37
38 system (Micromeritics ASAP 2050). Before the measurement, the sample was tableted, crushed,
39
40 weighed and reduced at 573 K in a flow of hydrogen for 4 h. A stainless steel tube was loaded
41
42 with 2 g of the reduced sample in a glovebox, and subsequently connected to the manometric
43
44 instrument. After pretreated under vacuum at 573 K for 2 h to remove water and other adsorbed
45
46 molecules, the sample was cooled down to the reaction temperature (473 K). Then, the H_2 was
47
48 injected into the sample tube to increase the pressure gradually to 5 MPa, for measuring the
49
50
51
52
53
54
55
56
57
58
59
60

1
2
3
4 pressure-composition-isotherms. The pressure was measured by a capacitance manometer with
5
6
7 an error of 1%.

8 9 **Computational details**

10
11
12 Monte Carlo simulations were carried out with the Adsorption Locator module implemented in
13
14 Materials Studio^{®18}. The adsorption configurations were identified by conducting Monte Carlo
15
16
17 searches of the configurational space of the substrate-adsorbate system¹⁹ as the temperature
18
19
20 slowly decreased according to a simulated annealing schedule.^{20,21} This process was repeated
21
22
23 several times to identify further local energy minima. Further details of Monte Carlo simulations
24
25
26 is shown in Supporting Information.

27 28 **RESULTS AND DISCUSSION**

29 30 31 **Morphology of NAHS materials with different nanotube-length**

32
33
34 The NAHS is formed by a dissolution-precipitation mechanism, which is shown in Figure S1.
35
36
37 At the early stage of hydrothermal treatment, the silica spheres dissolve and react with copper
38
39
40 ions to generate copper silicate. As the time of hydrothermal treatment increases, silica sphere
41
42
43 core continues to dissolve and more copper silicate generates, which prolongs the nanotubes.
44
45
46 And the nanotube would not stop growing until the copper ions were exhausted. Consequently,
47
48
49 nanotubes open-ended on both sides form a radial array on the surface of a hollow sphere,
50
51
52 providing the only connection between the space inside and outside of the hollow sphere (as
53
54
55 shown in Figure 1). The SEM images of cracked samples in Figure S4 shows that there is no
56
57
58 isolated nanotube existed inside the hollow spheres. According to the dissolution-precipitation
59
60

1
2
3
4 mechanism, we modulated the time of hydrothermal treatment and adjusted the copper content to
5
6 fabricate a series of NAHS materials with nanotubes of different lengths. The obtained samples
7
8 were characterized by TEM (Figure 1, corresponding large-scale TEM images and
9
10 high-magnification TEM images are shown in Figure S2 and S3). The length of the resulting
11
12 nanotubes varies from 63 nm to 119 nm as the hydrothermal time is increased from 5 h to 20 h.
13
14 As the amount of copper ions increases, the nanotube length further increases to 120 nm and 232
15
16 nm. The NAHS assembled with x nm nanotubes is denoted as NAHS- x nm. Additionally, copper
17
18 silicate nanotubes (NTs) and lamellar-structured Cu/SiO₂ were prepared as contrasting catalysts.
19
20 Notably, the nanotubes of NAHS-232nm are as long as the NTs, which enables a separate
21
22 discussion of the effect of nanotubes and hollow spheres. The copper silicate composition of all
23
24 the materials was verified by FTIR spectroscopy, as shown in Figure S5.
25
26
27
28
29
30
31
32
33

34 Figure S6 shows the nitrogen adsorption-desorption isotherms of copper silicate materials. All
35
36 the samples exhibit type IV isotherms with a hysteresis loop, corresponding to a typical
37
38 mesoporous material. The hysteresis loops of NAHS and NTs are attributed to the
39
40 cylinder-shaped pore,²² which is consisted with the shape of nanotube. Meanwhile, the hysteresis
41
42 loop of lamellar-structured Cu/SiO₂ is a standard H3 type loop, corresponding to the
43
44 lamellar-shaped pore.²³ These structures are also agreed with the structures shown in TEM
45
46 images (Figure 1). Furthermore, the specific surface area of the copper silicate materials (Table
47
48 S1) with same copper loadings is similar. The average pore size calculated by BJH method is
49
50 also shown in Table S1, indicating the pore size of all the materials is around 4.2 nm. This is also
51
52
53
54
55
56
57
58
59
60

confirmed by the high-magnification TEM images (Figure S3), where inner diameters of the nanotubes in both the NAHS and NTs are approximately 4 nm. We also counted the diameter of hollow sphere in all NAHS materials from lots of TEM images, which is all around 280 nm (Table S1). Thus, except for the length of nanotubes, all the NAHS samples display nearly the same pore structural properties, size of hollow spheres as well as diameter of nanotubes.

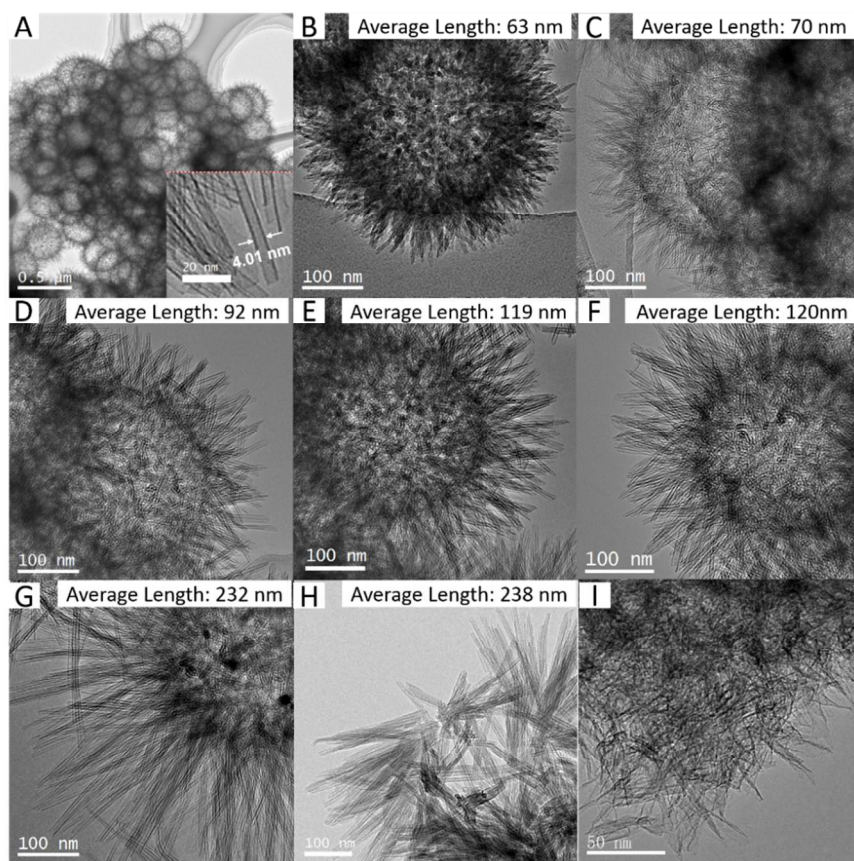


Figure 1. TEM images of calcined copper silicate materials. A-G: NAHS materials, H: NTs and I: lamellar-structured Cu/SiO₂. Copper contents: 20 wt. % (A-E), 43 wt. % (F-I). Hydrothermal treatment time: 5 h (B, F), 10 h (A, C), 15 h (D, H), 20 h (E, G). Corresponding large-scale TEM images and nanotube-length distributions are shown in Figure S2.

Morphology of NAHS nanoreactors

All the NAHS materials, NTs, and lamellar-structured Cu/SiO₂ were first reduced at 573 K in a H₂ flow for 4 h before the reaction. It can be seen from Figure 2 and Figure S7, although some of the lamellar-shaped Cu/SiO₂ turns to amorphous form, the structures of NAHS and NTs are not collapsed during reduction and there is no obvious pore on the nanotube wall. Meanwhile, the small nanoparticles generated in all the catalysts after reduction. The regular lattice with a interplanar spacing of 0.202 nm in Figure 2I can be ascribed to the Cu(111) phase of metallic Cu (JPCDS 65-9743), which is also consisted with the diffraction peak at 43.3° in XRD patterns (Figure 3(a)). The diameters of Cu nanoparticles are around 3 nm, which are calculated from the XRD patterns by Scherrer equation (Table 1). We also counted the metallic Cu particle sizes based on the TEM images (Table S2), which agree with the results from XRD patterns. Moreover, the magnified TEM image (Figure 2H) shows that most copper nanoparticles socket on the wall of nanotubes. In this case, part of the nanoparticle is exposed to the inside of nanotube and narrows the diameter of nanotube, which is consisted with the decreasing of the pore size of the NAHS nanoreactor after the reduction (Figure S9).

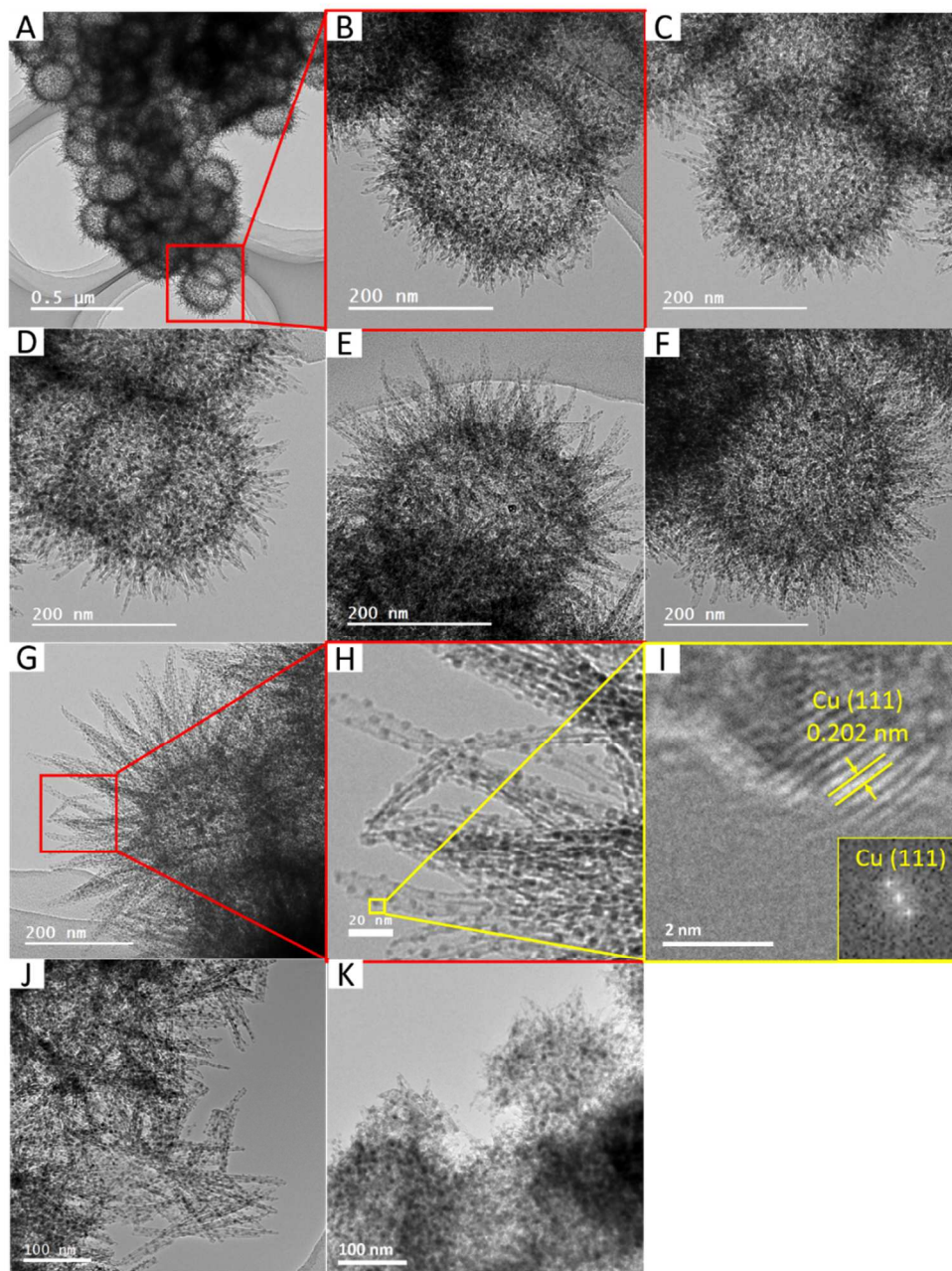
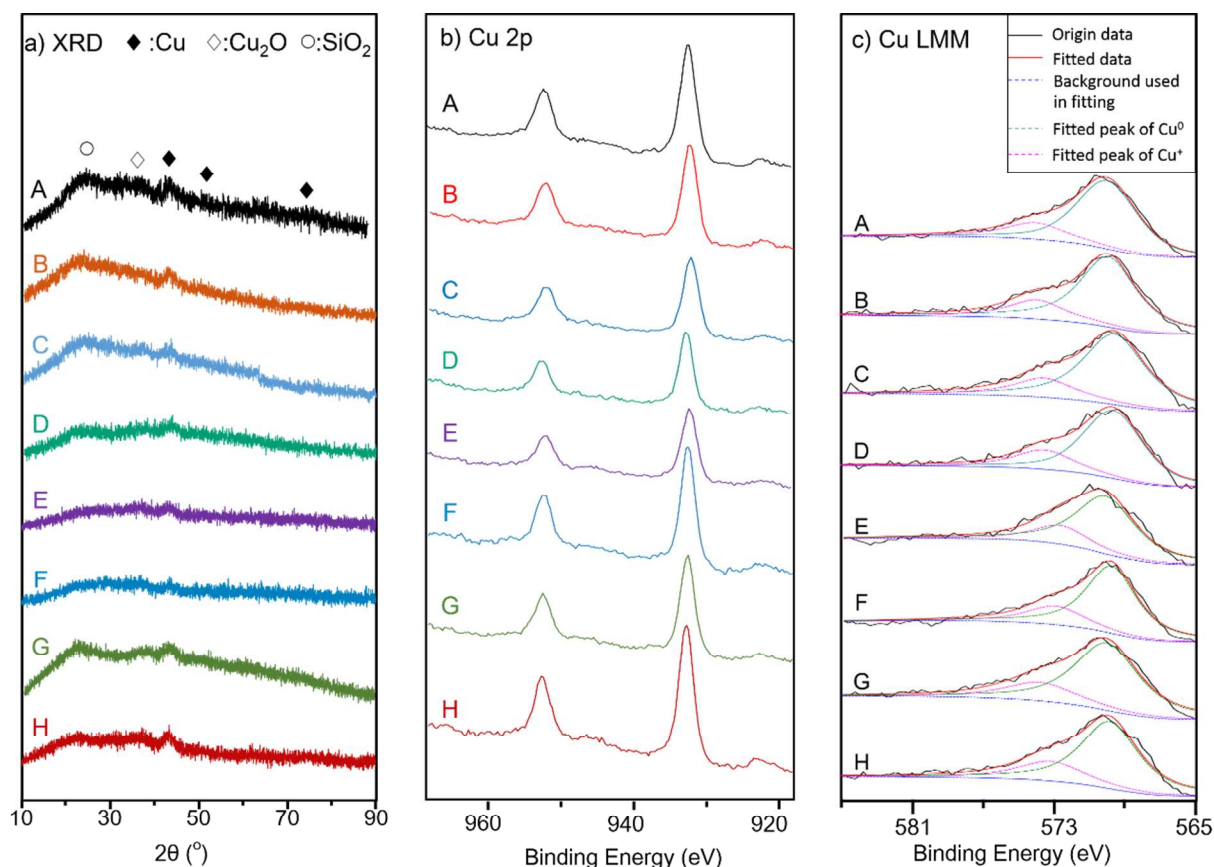


Figure 2. TEM images of reduced copper silicate materials. A, B: NAHS-63nm; C: NAHS-70nm; D: NAHS-92nm; E: NAHS-119nm; F: NAHS-120nm; G, H, I: NAHS-232nm, J: NTs and H: Cu/SiO₂. Corresponding large scale and high resolution TEM images are shown in Figure S7.

Characterization of active species

Considering the components, pore structure and copper particle size of all the catalysts are similar, the number of exposed active species may be the key factor influencing the catalytic performance, in addition to the morphology. The synergy between Cu^0 and Cu^+ species on the surface of catalysts has been reported to remarkably enhance the catalytic performance in DMO hydrogenation, where Cu^0 facilitates decomposition of H_2 and Cu^+ adsorbs and activates the methoxy or acyl species.²⁴⁻²⁶ Hence, we sequentially measured the surface amounts of Cu^0 and Cu^+ sites qualitatively and quantitatively. The Cu^0 surface areas ($S_{\text{Cu}(0)}$) of all the catalysts were determined by N_2O titration;^{27,28} the results are listed in Table 1. Notably, catalysts with the same Cu content display similar Cu^0 surface areas. The absence of the Cu 2p satellite peak at 942-944 eV in XPS (Figure 3) demonstrates that all of the surface Cu^{2+} species are reduced to a lower valence. In the absence of surface Cu^{2+} species, the surface area of Cu^0 and Cu^+ species could be distinguished and calculated by deconvoluting the two overlapping peaks at binding energies of 569.8 eV and 573.1 eV respectively in the Cu LMM AES (Figure 3). The ratio of $\text{Cu}^+ / (\text{Cu}^+ + \text{Cu}^0)$, denoted as $X_{\text{Cu}(I)}$, was calculated from the integrated areas of the corresponding peaks, as listed in Table 1.²⁵ The Cu^+ surface area ($S_{\text{Cu}(I)}$) was calculated on the basis of $S_{\text{Cu}(0)}$ and $X_{\text{Cu}(I)}$. Notably, the $\text{Cu}^+ / (\text{Cu}^+ + \text{Cu}^0)$ ratios of all the samples are similar, irrespective of their morphology. To further verify the fitting results of $X_{\text{Cu}(I)}$, in situ FTIR of CO adsorption was also conducted after CO adsorption (Figure S10). Given the weak interaction between CO and Cu^0 or Cu^{2+} , and the absence of Cu^{2+} of all the catalysts proved by XPS, the bands after long-time

1
2
3
4 evacuation at $2100\text{--}2200\text{ cm}^{-1}$ should be assigned to the $\text{Cu}^+\text{-CO}$ species.^{26, 29} The integral areas
5
6 of the $\text{Cu}^+\text{-CO}$ peaks are consistent with the calculated $S_{\text{Cu(I)}}$, verifying the reliability of the
7
8 characterizations of Cu^0 and Cu^+ species (Figure S10). In summary, considering that the
9
10 resemblance textural structure and active-site distribution of these catalysts, the contribution of
11
12 the morphology becomes the most important fact in catalyzing the hydrogenation reaction.
13
14
15
16



46 **Figure 3.** (a) XRD patterns (b) XPS spectra and (c) AES spectra of reduced copper silicate
47 materials. A: NAHS-63nm; B: NAHS-70nm; C: NAHS-92nm; D: NAHS-119nm; E:
48 NAHS-120nm; F: NAHS-232nm, G: NTs and H: Cu/SiO₂.
49
50
51
52
53
54
55
56
57
58
59
60

Table 1. Characterization of Cu species on catalysts.

Catalysts	Cu content ^a (wt. %)	Crystallite size ^b (nm)	S _{Cu(0)} ^c (m ² /g)	S _{Cu(I)} ^d (m ² /g)	X _{Cu(I)} ^e (%)
NAHS-63nm	19.8	3.2	27.1	7.9	22.6
NAHS-70nm	21.0	3.1	26.1	6.6	21.5
NAHS-92nm	20.3	3.0	25.7	7.3	22.2
NAHS-119nm	20.5	3.1	25.8	8.1	23.7
NAHS-120nm	41.7	3.2	42.9	12.9	23.0
NAHS-232nm	43.0	3.3	45.6	16.7	25.0
NAHS-232nm-used ^f	42.8	3.4	45.0	15.2	25.3
NTs	42.7	3.3	43.2	13.0	23.0
Cu/SiO ₂	43.9	3.8	45.0	14.6	24.2

^aDetermined by Inductively Coupled Plasma Optical Emission Spectrometry. ^bCalculated from XRD patterns by using the Scherrer equation. ^cDetermined by N₂O titration. ^dCalculated on the basis of S_{Cu(0)} and Cu⁺/(Cu⁺+Cu⁰) and verified by in-situ FTIR spectra of CO adsorption. ^eCalculated from Cu LMM AES spectra. ^f The NAHS-232nm-used catalyst is characterized after the 300 h long-time stability test.

Catalytic performance

To reveal the effects of morphology, the reduced NAHS-232nm nanoreactor, NTs and Cu/SiO₂ were evaluated in DMO hydrogenation under different H₂/DMO ratios (Figure 4 and S11). At the H₂/DMO ratio from 70 to 80, all three catalysts present nearly the same EG yields. When the H₂/DMO ratio is decreased from 70 to 50, the EG yield of Cu/SiO₂ decreases to 42% but that of the NAHS-232nm nanoreactor and NTs are maintained at 95%. As the H₂/DMO ratio is further

1
2
3
4 decreased below 50, a sharp decline of the EG yield appears in the activity tests of NTs. In
5
6 contrast, the NAHS-232nm nanoreactor continues to exhibit a high performance, with an EG
7
8 yield of 95% until the H₂/DMO ratio is decreased to 20. Moreover, the NAHS-232nm displays
9
10 excellent stability at H₂/DMO of 20, which is demonstrated by the 95% EG yield in 300 h
11
12 reaction (Figure 4C). During this long-time reaction, neither the structure of nanotubes nor the
13
14 hollow spheres of NAHS is obviously changed, which is demonstrated by the TEM image of the
15
16 used NAHS-232nm catalyst in Figure 4D. Furthermore, XRD (Figure S12A), XPS (Figure S12B,
17
18 C) and N₂O titration analysis of the used NAHS-232nm catalyst demonstrate that the copper
19
20 particle size and the surface areas of copper active species haven't changed as well after 300 h
21
22 reaction. These results of copper-species characterization of the used NAHS-232nm catalysts are
23
24 also summarized in Table 1.
25
26
27
28
29
30
31
32
33

34 For further understanding these different performance of catalysts, we used the Weisz-Prater
35
36 criterion³⁰ to evaluate the diffusion influence on this reaction. When the Weisz-Prater criterion is
37
38 less than 0.3, the effect of mass transfer of the reactant on reaction is negligible.³⁰ The calculated
39
40 N_{w-p} of DMO over NAHS-232nm, NTs and Cu/SiO₂ catalysts is much lower than the limit value
41
42 of 0.3, which is shown in Table S3. Thus the catalytic performance of these catalyst is not
43
44 limited by the mass transfer. As demonstrated before, the NAHS-232nm nanoreactor, NTs and
45
46 Cu/SiO₂ are all very similar in terms of their textural properties as well as the number of exposed
47
48 active sites, the diffusion limitation is also excluded by calculating the Weisz-Prater criterion
49
50
51
52
53
54
55
56
57
58
59
60

(Table S3)³⁰. The unique morphology of NAHS is the only key factor influencing catalytic performance in DMO hydrogenation.

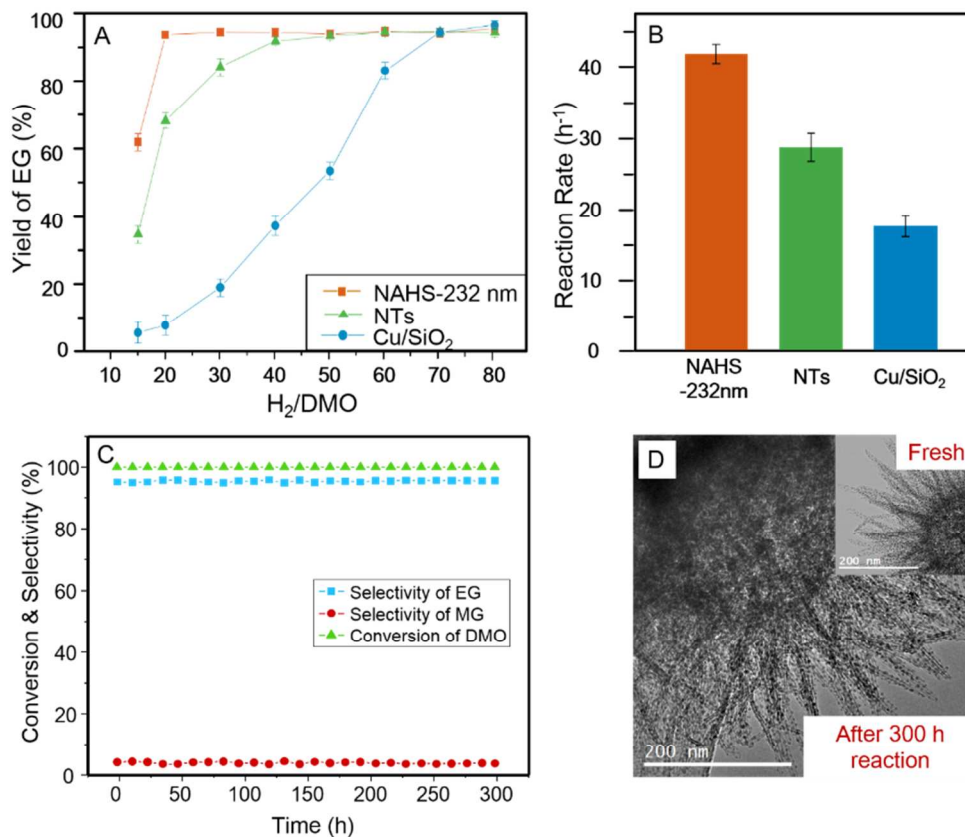


Figure 4. Comparison of catalytic performance. A: Effect of H₂/DMO ratio on the catalytic performance of different catalysts. Reaction conditions: 473 K, 2.5 MPa, WLHSV = 2.0 h⁻¹. B: Reaction rates of different catalysts at H₂/DMO = 20, 473 K, 2.5 MPa. The data for calculation of reaction rates were obtained under much more severe conditions, where the DMO conversions were kept below 20%. C: Stability test of NAHS-232nm nanoreactor. Reaction conditions: 473 K, 2.5 MPa, WLHSV = 2.0 h⁻¹, H₂/DMO = 20. D: TEM image of NAHS-232nm before and after 300 h reaction.

1
2
3
4 To further analyze the effect of morphology, we calculated the reaction rates as shown in
5
6 Figure 4B. The reactant concentration must be the main reason for the difference in reaction rates
7
8 because the three catalysts have identical distribution of active sites and reaction conditions.
9
10 Meanwhile, the TOF values (Figure S13) also show the same trend to the reaction rate because
11
12 the similar ratio of Cu^0/Cu^+ in these catalysts. Therefore, the morphology effect of the catalyst
13
14 results from its ability to be enriched by small molecules, as intended by our design.
15
16 Additionally, the reason of the slightly lower EG yield of NAHS-232nm is a further
17
18 hydrogenation of EG to other by-products. Compared against the current state-of-the-art
19
20 performance of the Cu/SiO_2 catalysts, this NAHS nanoreactor exhibits an excellent performance
21
22 in an extremely low H_2/DMO ratio (Table S4). Besides DMO hydrogenation, the NAHS
23
24 nanoreactor also exhibits an excellent performance under a low H_2 proportion in other $\text{C}=\text{O}/\text{C}-\text{O}$
25
26 hydrogenation reactions, which is shown in Figure S14. The results indicate that the morphology
27
28 of NAHS could be generalized into other hydrogenation reactions.
29
30
31
32
33
34
35
36
37
38

39 **Enrichment of H_2 inside NAHS**

40
41
42 To gain further insight into the morphology effect, the H_2 -adsorption volumes of the three
43
44 catalysts were investigated at the reaction temperature of 473 K. The relation between the H_2
45
46 pressure and the adsorption volumes of the reduced NAHS-232nm nanoreactor, NTs and
47
48 Cu/SiO_2 catalysts is shown in Figure 5. At the reaction pressure of 2.5 MPa, the H_2 -adsorption
49
50 volume of the NAHS-232nm nanoreactor is 51.80 mL/g, higher than the adsorption volumes of
51
52 the NTs (39.20 mL/g) and Cu/SiO_2 (21.47 mL/g). The difference between the H_2 -adsorption
53
54
55
56
57
58
59
60

volumes of these catalysts becomes much larger as the pressure is increased. The results indicate that both nanotube and hollow-sphere morphologies can enhance the adsorption of H₂. This effect of enrichment may increase the local concentration of H₂ around the active sites, resulting in an accelerated reaction rate and an improved catalytic performance.

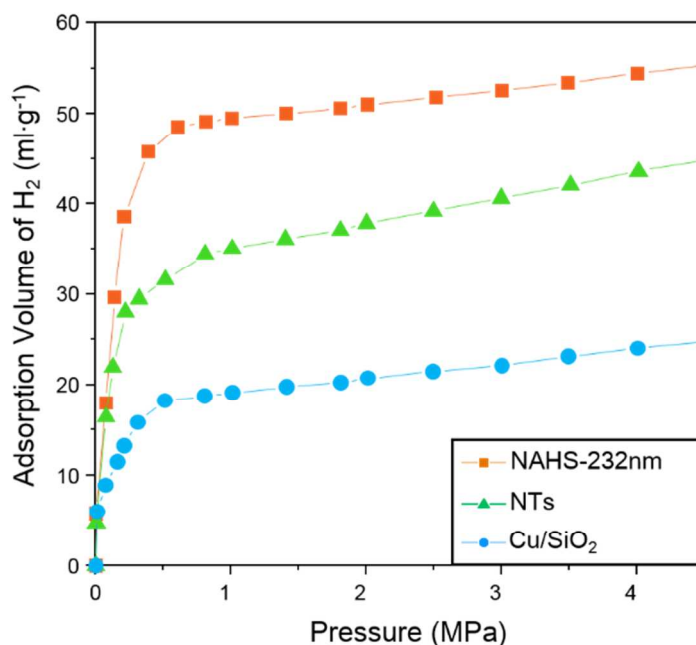


Figure 5. H₂-adsorption isotherms of the NAHS materials, NTs and Cu/SiO₂ catalysts.

Adsorption temperature: 473 K.

Furthermore, Monte Carlo simulations were also employed to further elucidate the phenomenon of H₂-enrichment in the nanotube morphology. A silica nanotube was modeled with a nanotube morphology in NAHS nanoreactors and NTs, whereas a planar counterpart was selected to represent the surface of the Cu/SiO₂ catalyst (Figure 6B-C, Figures S15 and S16). Both models are placed in quadrilateral boxes aligned periodically in three dimensions. Local

1
2
3
4 concentrations of H₂ molecules inside/outside of the nanotube, or around the planar surface were
5
6
7 calculated. Results obtained in the reaction temperature of 473 K, and with different H₂
8
9 pressures, are shown in Figure 6A. Local concentrations of H₂ molecules decrease in the
10
11 following order: inside the nanotube, around the planar surface, in the gas phase, and outside the
12
13 nanotube. This order implies the significant enrichment effect inside the nanotube structure. Due
14
15 to the unique geometry of curved surface of nanotubes, the Si and O atoms on the concave side
16
17 are denser than those on the convex side. Thus, the H₂ molecules interact more strongly with the
18
19 concave surface than with the convex surface when the distances are equal. The good adsorption
20
21 ability on the concave side probably causes the enrichment effect of H₂ on the nanotubes.^{31, 32}
22
23 Moreover, the silica hollow sphere structure has previously been shown to store more guest
24
25 molecules (like CO₂, ibuprofen or hexane) than conventional mesoporous materials such as
26
27 MCM-41, SBA-15 or HMS.^{33, 34} In the present study, the NAHS nanoreactors, which contain
28
29 both nanotube and hollow-sphere structures, exhibit a much superior H₂-enrichment effect than
30
31 the NTs and Cu/SiO₂. Consequently, the H₂/DMO ratio inside the NAHS nanoreactors is
32
33 probably higher than that in the gas phase, which is the reason that the nanoreactor maintains
34
35 excellent activity even at a low H₂/DMO ratio in the feed.
36
37
38
39
40
41
42
43
44
45
46
47
48
49
50
51
52
53
54
55
56
57
58
59
60

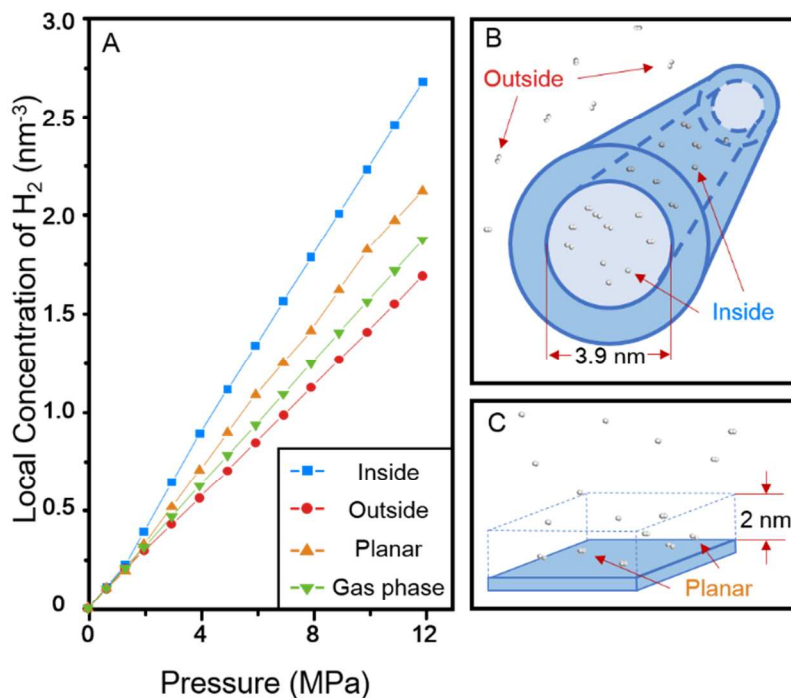


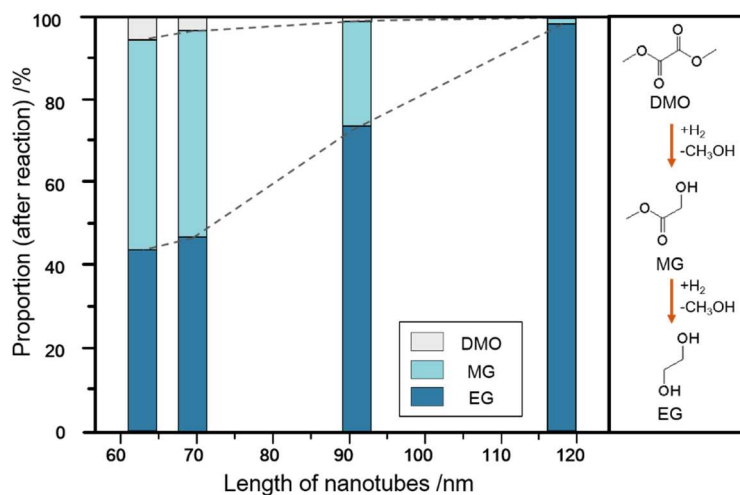
Figure 6. A: Local concentrations of H₂ inside nanotubes, outside nanotubes and around planar surface, calculated by Monte Carlo simulations at 473 K. B: Model of silica nanotube. C: Model of silica planar surface. The H₂ molecules within 2 nm of the silica surface, which is equal to the radius of the nanotube, are considered as the molecules near the planar surface.

Spatial restriction of reactants inside NAHS

To explore the spatial restriction of nanotubes, NAHS nanoreactors with identical Cu contents, but different nanotube lengths, were also evaluated in DMO hydrogenation. To ensure the presence of sufficient H₂ and to exclude the enrichment effect, a H₂/DMO ratio of 70 was used.

As shown in Figure 7, as the nanotube length is increased from 63 to 119 nm, the conversion of DMO increases and more MG is hydrogenated to EG, which exhibits an increase of EG selectivity. Due to the similarity of the textural properties, number of exposed active sites and

1
2
3
4 morphologies of these nanoreactors (Table 1), the variation in nanotube length must be the
5
6
7 reason for the difference in product distribution. This spatial restriction, due to the nanotube
8
9
10 shell, may enhance the probability of contact between the molecules and the active sites. Thus,
11
12 the NAHS nanoreactor with longer nanotubes would catalyze the hydrogenation reaction with a
13
14 higher performance. Taking into account this spatial restriction effect of NAHS nanoreactors,
15
16
17 control of the nanotube length could be an effective way to manipulate the selectivity and
18
19
20 product distribution in hydrogenation.
21



22
23
24
25
26
27
28
29
30
31
32
33
34
35
36
37
38
39
40 **Figure 7.** Comparison of product distribution of NAHS nanoreactors with different lengths of
41
42 nanotubes. Reaction conditions: 473 K, 2.5 MPa, WLHSV = 2.0 h⁻¹, H₂/DMO = 70.
43
44

45 CONCLUSIONS

46
47
48 In this work, we propose a novel nanoreactor with a unique morphology of
49
50 nanotube-assembled hollow sphere, which can exhibit remarkable activity and stability when the
51
52 H₂ dosage in C=O/C-O hydrogenation reaction is significantly decreased. To obtain an EG yield
53
54
55
56
57
58
59
60

1
2
3
4 of 95%, the NAHS nanoreactor could allow the H₂/DMO ratio to be decreased to 20, while the
5
6
7 NTs and Cu/SiO₂ require at least a H₂/DMO ratio of 50 and 70, respectively. Given the similar
8
9
10 textural structure and active-site distribution of these catalysts, the contribution of the
11
12 morphology in catalyzing the hydrogenation reaction is revealed. Both the experimental and
13
14
15 computational results demonstrate that the structure of nanotube and hollow sphere could
16
17
18 increase the hydrogen concentration within the nanoreactor, resulting in the excellent activity of
19
20
21 NAHS at low H₂ proportion in DMO hydrogenation, as well as other hydrogenations. Moreover,
22
23
24 when the nanotubes on the NAHS are lengthened, DMO is hydrogenated to a further stage,
25
26
27 resulting in selective production of EG. Therefore, the NAHS nanoreactor proposed here
28
29
30 provides a promising solution for both of the imperative issues in hydrogenation reactions:
31
32
33 excess H₂ consumption and the control of product selectivity. Based on these insights into the
34
35
36 effect of morphology on hydrogen enrichment and the effect of spatial restriction on catalytic
37
38
39 performance, new possibilities can be introduced for the rational design of catalysts.
40
41
42
43
44
45
46
47
48
49
50
51
52
53
54
55
56
57
58
59
60

1
2
3
4 **AUTHOR INFORMATION**
5

6
7 **Corresponding Author**
8

9
10 *E-mail: xbma@tju.edu.cn
11
12

13
14 **Author Contributions**
15

16 ‡D. Y. and Y. W. contributed equally to this whole work.
17
18

19
20 **Notes**
21

22
23 The authors declare no competing financial interest.
24
25

26
27 **ASSOCIATED CONTENT**
28

29
30 Details of experiments, catalyst characterization and evaluation, Monte Carlo simulations are
31 included in Supporting Information. The Supporting Information is available free of charge on
32 the ACS Publications website.
33
34
35
36
37

38
39 **ACKNOWLEDGMENT**
40

41
42 This work was supported by the National Natural Science Foundation of China (21325626,
43 91434127).
44
45
46
47
48
49
50
51
52
53
54
55
56
57
58
59
60

1
2
3
4 **REFERENCES**
5

- 6 (1) Klankermayer, J.; Wesselbaum, S.; Beydoun, K.; Leitner, W. *Angew. Chem. Inter. Ed.*
7 **2016**, *55*, 7296-7343.
8
9
10
11
12 (2) Ruppert, A.; Weinberg, K.; Palkovits, R. *Angew. Chem. Inter. Ed.* **2012**, *51*, 2564-2601.
13
14
15
16 (3) Yue, H.; Ma, X.; Gong, J. *Acc. Chem. Res.* **2014**, *47*, 1483-1492.
17
18
19
20 (4) Zhao, S.; Yue, H.; Zhao, Y.; Wang, B.; Geng, Y.; Lv, J.; Wang, S.; Gong, J.; Ma, X. *J.*
21
22 *Catal.* **2013**, *297*, 142-150.
23
24
25
26 (5) Yin, A.; Wen, C.; Guo, X.; Dai, W.; Fan, K. *J. Catal.* **2011**, *280*, 77-88.
27
28
29
30 (6) Zhao, L.; Zhao, Y.; Wang, S.; Yue, H.; Wang, B.; Lv, J.; Ma, X. *Ind. Eng. Chem. Res.*
31
32 **2012**, *51*, 13935-13943.
33
34
35
36 (7) Chen, L.; Guo, P.; Qiao, M.; Yan, S.; Li, H.; Shen, W.; Xu, H.; Fan, K. *J. Catal.* **2008**,
37
38 *257*, 172-180.
39
40
41
42 (8) Hollak, S.; Gosselink, R.; van Es, D.; Bitter, J. *ACS Catal.* **2013**, *3*, 2837-2844.
43
44
45
46 (9) Maligal-Ganesh, R.; Xiao, C.; Goh, T.; Wang, L.; Gustafson, J.; Pei, Y.; Qi, Z.;
47
48 Johnson, D.; Zhang, S.; Tao, F.; Huang, W. *ACS Catal.* **2016**, *6*, 1754-1763.
49
50
51
52 (10) Bai, S.; Liu, J.; Gao, J.; Yang, Q.; Li, C. *Microporous Mesoporous Mater.* **2012**, *151*,
53
54 474-480.
55
56
57
58
59
60

- 1
2
3
4 (11) Wang, X.; Zhuang, J.; Chen, J.; Zhou, K.; Li, Y. *Angew. Chem. Inter. Ed.* **2004**, 43,
5
6
7 2017-2020.
8
9
10 (12) Yue, H.; Zhao, Y.; Zhao, S.; Wang, B.; Ma, X.; Gong, J. *Nat. Commun.* **2013**, 4, 2339.
11
12
13 (13) Bao, J.; He, J.; Zhang, Y.; Yoneyama, Y.; Tsubaki, N. *Angew. Chem. Inter. Ed.* **2008**,
14
15
16 47, 353-356.
17
18
19 (14) Yang, Y.; Liu, X.; Li, X.; Zhao, J.; Bai, S.; Liu, J.; Yang, Q. *Angew. Chem. Inter. Ed.*
20
21
22 **2012**, 51, 9164-9168.
23
24
25 (15) Gong, J.; Yue, H.; Zhao, Y.; Zhao, S.; Zhao, L.; Lv, J.; Wang, S.; Ma, X. *J. Am. Chem.*
26
27 *Soc.* **2012**, 134, 13922-13925
28
29
30 (16) Wang, Y.; Wang, G.; Wang, H.; Cai, W.; Zhang, L. D., *Chem. Commun.* **2008**,
31
32
33 6555-6557.
34
35
36 (17) Sheng, Y.; Zeng, H. C. *Chem. Mat.* **2015**, 27, 658-667.
37
38
39 (18) Metropolis, N.; Rosenbluth, A. W.; Rosenbluth, M. N.; Teller, A. H.; Teller, E. *J. Chem.*
40
41
42 *Phys.* **1953**, 21, 1087.
43
44
45 (19) Frenkel, D.; Smit, B. In *Understanding Molecular Simulation: From Algorithms to*
46
47
48 *Applications*, 2nd ed.; Academic Press: San Diego, 2002.
49
50
51 (20) Kirkpatrick, S.; Gelatt, C. D.; Vecchi, M. P. *Science*, **1983**, 220, 671-680.
52
53
54 (21) Cerný, V. *J. Optim. Theor. Appl.*, **1985**, 45, 41-51.
55
56
57
58
59
60

1
2
3
4 (22) Kondo, S.; Ishikawa, T.; Abe, I. In *Adsorption Science*, 2nd ed.; Chemical Industry
5
6 press: Beijing, 2005; p 69.

7
8
9
10 (23) Sing, K.; Everett, D.; Hau, R.; Moscou, L.; Pierott, R.; Rouquerol, J.; Siemieniewska, T;
11
12 *Pure Appl. Chem.* **1985**, *57*, 603-615

13
14
15
16 (24) Yin, A.; Guo, X.; Dai, W.; Fan, K. *J. Phy. Chem. C* **2009**, *113*, 11003-11013.

17
18
19
20 (25) Li, S.; Wang, Y.; Zhang, J.; Wang, S.; Xu, Y.; Zhao, Y. J.; Ma, X. *Ind. Eng. Chem. Res.*
21
22 **2015**, *54*, 1243-1250.

23
24
25
26 (26) Wang, Y.; Shen, Y.; Zhao, Y.; Lv, J.; Wang, S.; Ma, X. *ACS Catal.* **2015**, *5*, 6200-6208.

27
28
29
30 (27) Chinchin. G.; Hay. C.; Vandervell. H.; Waugh. K. *J. Catal.* **1987**, *103*, 79-86.

31
32
33 (28) Zhu, Y.; Kong, X.; Li, X.; Ding, G.; Zhu, Y.; Li, Y. *ACS Catal.* **2014**, *4*, 3612-3620.

34
35
36
37 (29) Zheng, J.; Zhou, J.; Lin, H.; Duan, X.; Williams, C.; Yuan, Y. *J. Phy. Chem. C* **2015**,
38
39 119, 13758-13766.

40
41
42
43 (30) Albert. M. In *Kinetics of Catalytic Reaction*, 1st ed; Springer: Pennsylvania State, 2005;
44
45 p 63.

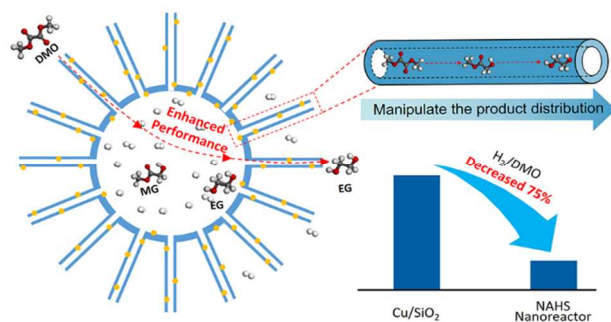
46
47
48
49 (31) Guan, J.; Pan, X.; Liu, X.; Bao, X. *J. Phys. Chem. C* **2009**, *113*, 21687-21692.

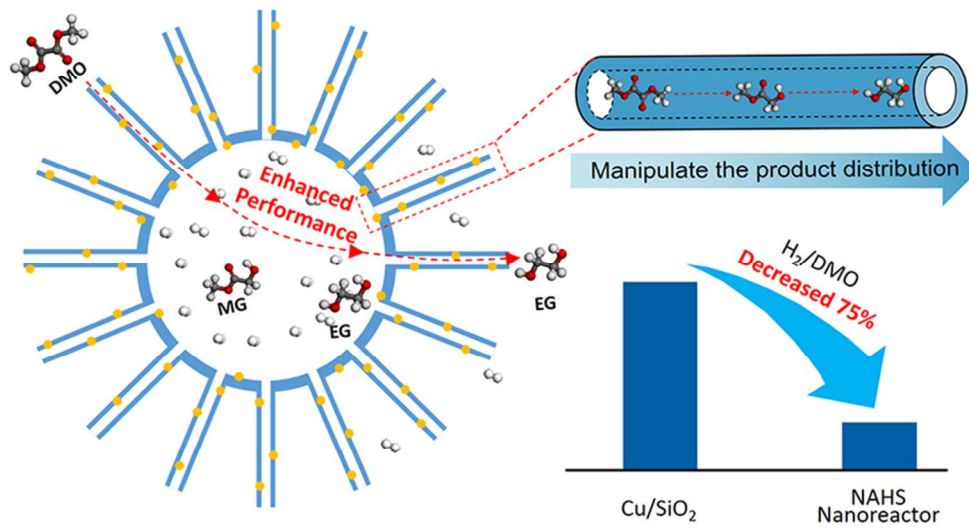
50
51
52
53 (32) Hussain, M.; Vijay, D.; Sastry, G. *J. Comput. Chem.* **2016**, *37*, 366-377.

1
2
3
4 (33) Lin, L.; Bai, H., *Microporous Mesoporous Mater.* **2013**, 170, 266-273.
5
6

7 (34) Zhu, Y.; Shi, J.; Chen, H.; Shen, W.; Dong, X. *Microporous Mesoporous Mater.* **2005**,
8
9
10 84, 218-222.
11
12
13
14
15
16
17
18
19
20
21
22
23
24
25
26
27
28
29
30
31
32
33
34
35
36
37
38
39
40
41
42
43
44
45
46
47
48
49
50
51
52
53
54
55
56
57
58
59
60

TOC Graphic





84x47mm (300 x 300 DPI)